

# FCaS: Fine-grained Cardiac Image Synthesis based on 3D Template Conditional Diffusion Model

Jiahao Xia<sup>1,\*</sup>, Yutao Hu<sup>1,\*</sup>, Yaolei Qi<sup>1</sup>, Zhenliang Li<sup>1</sup>, Wenqi Shao<sup>4</sup>, Junjun He<sup>4</sup>,  
Ying Fu<sup>5</sup>, Longjiang Zhang<sup>6,†</sup>, Guanyu Yang<sup>1,2,3,†</sup>

<sup>1</sup>Key Laboratory of New Generation Artificial Intelligence Technology and Its Interdisciplinary Applications (Southeast University), Ministry of Education, China

<sup>2</sup>Jiangsu Province Joint International Research Laboratory of Medical Information Processing, Southeast University, Nanjing, China

<sup>3</sup>Univ Rennes, CHU Rennes, Inserm, LTSI– UMR 1099, F-35000 Rennes, France

<sup>4</sup>Shanghai AI Laboratory

<sup>5</sup>School of Computer Science and Technology, Beijing Institute of Technology, Beijing, China

<sup>6</sup>Department of Radiology, Jinling Hospital, Affiliated Hospital of Medical School, Nanjing University, Nanjing, China

## Abstract

Solving medical imaging data scarcity through semantic image generation has attracted significant attention in recent years. However, existing methods primarily focus on generating whole-organ or large-tissue structures, showing limited effectiveness for organs with fine-grained structure. Due to stringent topological consistency, fragile coronary features, and complex 3D morphological heterogeneity in cardiac imaging, accurately reconstructing fine-grained anatomical details of the heart remains a great challenge. To address this problem, in this paper, we propose the Fine-grained Cardiac image Synthesis (FCaS) framework, established on 3D template conditional diffusion model. FCaS achieves precise cardiac structure generation using Template-guided Conditional Diffusion Model (TCDM) through bidirectional mechanisms, which provides the fine-grained topological structure information of target image through the guidance of template. Meanwhile, we design a deformable Mask Generation Module (MGM) to mitigate the scarcity of high-quality and diverse reference mask in the generation process. Furthermore, to alleviate the confusion caused by imprecise synthetic images, we propose a Confidence-aware Adaptive Learning (CAL) strategy to facilitate the pre-training of downstream segmentation tasks. Specifically, we introduce the Skip-Sampling Variance (SSV) estimation to obtain confidence maps, which are subsequently employed to rectify the pre-training on down-

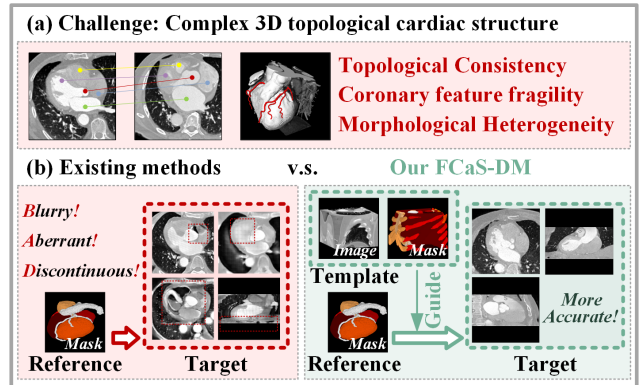


Figure 1. (a) **Challenges:** Topological consistency, coronary feature fragility, and morphological heterogeneity pose significant challenges to the precise generation of cardiac images. (b) **Innovation:** Beyond only using the segmentation mask as a reference, our FCaS incorporates the cardiac template as an additional information to guide the generation process, bringing the more precise and continuous volumetric synthetic image and overcoming the **BAD** outputs observed with existing methods[1, 20, 36].

stream tasks. Experimental results demonstrate that images generated from FCaS achieves state-of-the-art performance in topological consistency and visual quality, which significantly facilitates the downstream tasks as well. Code will be released in the future.

## 1. Introduction

Cardiovascular disease is one of the most severe diseases worldwide, and its accurate diagnosis is crucial for patient

\*Equal contribution.

†Corresponding author.

treatment and prognosis[27]. In recent years, the advancement of artificial intelligence (AI) has created new opportunities to enhance diagnostic efficiency and accuracy. However, training AI models for cardiovascular disease diagnosis relies on the numerous training data[16]. Nevertheless, obtaining cardiac image with high-quality annotation is extremely expensive and labor-intensive[6, 17, 56]. This issue is further compounded in the segmentation task. Due to the complex topology of cardiac structures, inter-individual morphological variations[13, 38, 40], it is difficult to obtain precise voxel-level annotations. Consequently, there is an urgent need to develop advanced methods for synthesizing cardiac images with high-quality masks, which could strongly facilitate the down-stream data-driven tasks.

Although recent robust AIGC models have demonstrated remarkable capabilities in image synthesis within the general vision domain, they fall short in the realm of medical image generation due to inherent dimensional and non-linear complexities [6, 34]. Recent years have witnessed significant efforts in medical image generation to achieve more precise synthesis results. Some researchers[1, 3, 5, 22, 34] have explored incorporating various guidance signals (*e.g.*, textual descriptions, electrocardiograms, masks) that provide medical prior knowledge to improve the generation process. Among them, while mask-guided semantic image synthesis algorithms[1] have achieved notable progress in 2D medical modalities, the high demands of continuity in 3D medical image mean that features learned in 2D space are insufficient for comprehensive representation. Recently, some methods[7, 10, 45] transfer successful experiences from 2D to design advanced 3D generative models, which demonstrate better spatial continuity.

However, the aforementioned methods cannot generate the high-quality cardiac computed tomography angiography (CTA) images, which has been proven high effectiveness in diagnosing cardiovascular disease. As shown in Fig. 1, the challenges could be summarized from three aspects: (1) **Topological consistency**: Cardiac imaging has stringent and precise spatial relationships between chambers and vessels[41]. Unguided generations often suffer from structural distortions and stochastic artifacts, failing to meet such complex requirements. (2) **Coronary feature fragility**: Coronary arteries constitute minimal anatomical proportions[39], causing generative models to neglect the subtle yet critical vascular elements. (3) **Morphological heterogeneity**: Cardiac structures exhibit extensive morphological diversity due to inter-subject variations or pathological conditions[14]. As a result, the precise generation of cardiac images remains an unresolved issue.

To address the above obstacles and synthesize high-quality cardiac CTA images, this paper proposes a novel **Fine-grained Cardiac image Synthesis** framework based on 3D template conditional diffusion model (FCaS). Specifi-

cally, to accommodate the complex topology of the heart, we design a **Template-guided Conditional Diffusion Model (TCDM)**, which incorporates the fine-grained reference mask with template pair as conditions. Within the TCDM, we present a bidirectional training strategy to maximize data utility, where two data pairs alternately serve as template pair and reference-target pair. Moreover, to mitigate the scarcity of high-quality segmentation masks, we utilize a **Mask Generation Module (MGM)** to obtain diverse topology-preserved masks when the available masks are not sufficient for the image synthesis. Meanwhile, we propose an innovative downstream pre-training strategy called **Confidence-aware Adaptive Learning (CAL)** to dynamically adjust the contribution of each spatial voxel of synthetic data. Specifically, we introduce the **Skip-Sampling Variance (SSV)** estimation to generate confidence maps, which serve as the dynamic weights of downstream training loss function. Generally speaking, extensive experiments demonstrate that, our FCaS achieves remarkable quality improvements in cardiac image synthesis and facilitates the downstream segmentation pre-training.

The key contributions of this work are:

- We present a cardiac image synthesis framework, named as FCaS. To our best knowledge, FCaS is the first approach to generate fine-grained and high-quality cardiac image with topological details preserved, which significantly alleviates the scarcity of medical image with mask annotations in the cardiac domain.
- We propose a 3D Template-guided Conditional Diffusion Model (TCDM), which utilizes fine-grained masks and template data to provide precise structure, thereby effectively guiding the diffusion model for synthesis. Meanwhile, the Mask Generation Module (MGM) is also incorporated to generate numerous topology-preserved reference masks, which facilitates the diverse generation.
- We develop a novel segmentation pre-training strategy, Confidence-aware Adaptive Learning (CAL), which incorporates Skip-Sampling Variance (SSV) estimation to generate confidence maps. By providing dynamic weight for the loss function, the confidence map greatly enhances learning efficiency and robustness for pre-training.
- Extensive experimental results demonstrate that our FCaS achieves superior image quality assessment metrics, and obtains significant performance improvements in downstream segmentation pre-training.

## 2. Related Work

### 2.1. Semantic Image Synthesis

Semantic image synthesis utilizes mask semantics and spatial information to guide the generative model, producing diverse images that inherently include segmentation

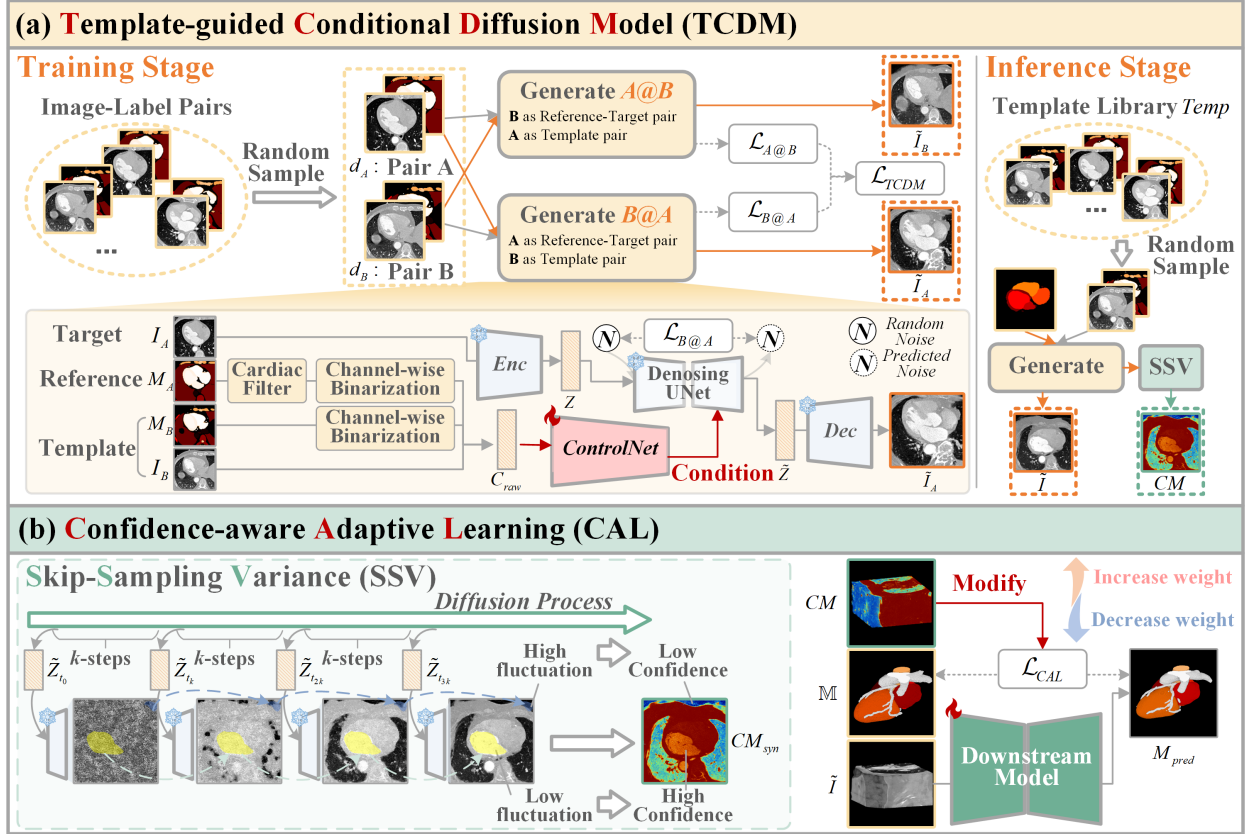


Figure 2. Overview of the proposed Fine-grained Cardiac image Synthesis framework. (a) The Template-guided Conditional Diffusion Model (TCDM) is designed to generate the precise, diverse, and topology-preserved cardiac images based on template-guided conditions. (b) The Confidence-aware Adaptive Learning (CAL) aims to modify the downstream segmentation pre-training by using confidence maps.

masks, thereby offering valuable annotated data for downstream segmentation tasks. The pioneering pix2pix[20] framework establishes a foundational paradigm for mask-to-image mapping using Generative Adversarial Networks (GANs). Subsequent advancements[36] further refine semantic representation capacity through enhanced network architectures. Tan *et al.*[43] and Wang *et al.*[48] later achieve breakthroughs by analyzing semantic probability distributions and decoupling semantic content from style information, showing considerable improvements across multiple tasks. More recent explorations[2, 21, 28, 29, 44, 54] have expanded research frontiers into 3D scene reconstruction, object arrangement optimization, model efficiency enhancement, and Transformer-based architectures.

The advent of diffusion models[15], characterized by their iterative denoising generation process, has showcased formidable generative capabilities that bolster semantic image synthesis tasks. Some works such as ControlNet[55], InstantID[47], T2I-Adapter[32] and StableSketching[26] demonstrate that incorporating rich prompt such as Canny edges, segmentation masks, and sketches enables generation of high-quality images that meet specific requirements.

However, directly applying these methods to 3D cardiac

imaging poses significant challenges. Specifically, there are difficulties in generating intricate anatomical details while ensuring topological consistency within the complex spatial constraints of 3D environments.

## 2.2. Medical Image Generation

Medical image generation coupled with synthetic data-based pre-training represents a crucial paradigm for addressing data scarcity in medical imaging. Recent advancements have explored various generative approaches including unconditional synthesis, conditional generation, and multi-modal fusion, aiming to produce diverse and realistic medical images. Due to heterogeneous acquisition difficulties across imaging modalities, researchers have developed cross-modal conversion techniques[30, 37] and super-resolution reconstruction algorithms [18, 25]. Notably, some works[1, 4, 22, 35] claim that incorporating attention maps, class labels, and tumor masks as conditional inputs significantly improves generation quality compared to unguided methods, particularly in localized synthesis.

Müller-Franzes *et al.*[33] experimentally validate that slower synthesis speed of diffusion models is justified by superior image quality in medical contexts. Han *et al.*[12]

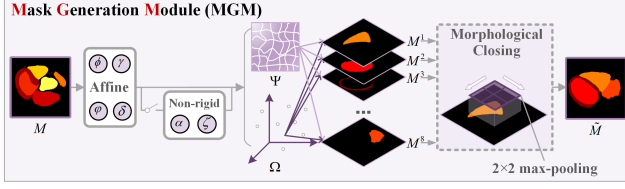


Figure 3. The workflow of Mask Generation Module.

achieve 3D reconstruction by aggregating multi-view 2D slices. Meanwhile, Other studies[7, 10, 45, 51] pioneer high-resolution 3D training through various resizing or cropping strategies. Moreover, some researchers[23, 24, 27, 46] have further advanced this field by demonstrating that synthetic medical images can effectively promote the performance of downstream tasks particularly when real data is scarce.

However, existing methods still remain unsatisfactory in generating fine-grained 3D cardiac images with topological consistency. To overcome these limitations, we propose the FCaS framework, which precisely synthesizes cardiac images while simultaneously generating confidence maps, facilitating more effective pre-training for downstream segmentation tasks.

### 3. Methodology

This section presents a comprehensive overview of the proposed FCaS framework. As shown in Fig. 2, the architecture comprises two principal components, TCDM and CAL strategy. The TCDM aims to generate high-quality synthetic images with template-guided conditions, and the CAL strategy is designed to achieve better pre-training performance on segmentation tasks. We will elaborate on these two important components in detail in the following parts.

#### 3.1. Template-guided Conditional Diffusion Model

##### 3.1.1. Semantic Reference with Template Guidance

During the training phase, two data pairs  $d_A = \{I_A, M_A\}$  and  $d_B = \{I_B, M_B\}$  are sampled from the training set  $D^{tr} = \{d_i^{tr}\}_{i=1}^{N^{tr}}$ . After spatial resampling, all volumes  $I_A, M_A, I_B, M_B \in \mathbb{R}^{D \times H \times W}$  are standardized to the same size and then fed into the generator as inputs, adopting two distinct patterns:  $A@B$  and  $B@A$ , respectively. Taking the generation direction  $B@A$  as an example, pair B is regarded as template pair while  $I_A$  and  $M_A$  are utilized as reference and target, respectively.  $M_A, I_B$ , and  $M_B$  collectively provide spatial structure condition to prompt the synthesis of  $I_A$ . We maintain the  $M_B$  unchanged, while  $M_A$  is filtered to exclude non-cardiac regions, thereby enabling the model to prioritize cardiac structures (coronary arteries, ascending aorta, left atrium, left ventricle, right atrium, right ventricle, left myocardium, and pulmonary artery).

Ensuring adequate mask representation while avoiding

computational overcost, inspired by MAISI[10], we implement channel-wise binarization for masks  $M_A$  and  $M_B$  to obtain  $M'_A$  and  $M'_B$ . We then concatenate them with the template image  $I_B$  to form the raw condition feature  $c_{raw} = M'_A \textcircled{C} M'_B \textcircled{C} I_B \in \mathbb{R}^{C \times D \times H \times W}$ , where  $\textcircled{C}$  denotes the concatenation along the channel axis. The final condition feature  $c$ , which guides the synthesis process of  $I_A$ , is encoded by a trainable ControlNet module  $E_{ctrl}$ . The process can be defined as follows:

$$c = E_{ctrl}(c_{raw}). \quad (1)$$

For the generation target  $I_A$ , we first obtain the latent space encoding feature  $Z \in \mathbb{R}^{4 \times \frac{D}{4} \times \frac{H}{4} \times \frac{W}{4}}$  via a pre-trained encoder with frozen parameters. The diffusion model iteratively adds random noise by  $Z_t = \sqrt{1 - \beta_t} Z_{t-1} + \sqrt{\beta_t} \epsilon_t$  to obtain  $Z \sim \mathcal{N}(0, 1)$ , where  $\beta_t$  is used to control the diffusion process. Then we sample  $\tilde{Z}_T$  from pure Gaussian noise and sample  $\tilde{Z}_0$  by denoising following Eq. (2).

$$p_{\theta}(\tilde{Z}_{t-1} | \tilde{Z}_t) = \mathcal{N}(\tilde{Z}_{t-1}; \mu_{\theta}(\tilde{Z}_t, t), \Sigma_{\theta}(\tilde{Z}_t, t)) \quad (2)$$

Using condition feature  $c$  as guidance, we integrate time embedding  $t$  and current state  $\tilde{Z}_t$  into a denoising model to predict noise  $\tilde{\epsilon}_t$ . Subsequently, we compute the distance between  $\tilde{\epsilon}_t$  and real noise  $\epsilon_t$  as the training objective:

$$\mathcal{L}_{DM} = \mathbb{E}_{\tilde{Z}_0, \epsilon_t \sim \mathcal{N}(0,1), t, c} \left[ \left\| \epsilon_t - \tilde{\epsilon}_t(\tilde{Z}_t, t, c) \right\|_2^2 \right], \quad (3)$$

where  $\tilde{Z}_0$  represent the clean latent feature at step 0 of the reverse diffusion process. Then  $\tilde{Z}_0$  will be decoded into synthetic Image  $I_A$  by a decoder.

##### 3.1.2. Bidirectional Training Strategy

Our proposed template-guided model necessitates the simultaneous loading of two data pairs  $d_A = \{I_A, M_A\}$  and  $d_B = \{I_B, M_B\}$ . Therefore, we introduce a bidirectional training strategy that aligns with the structural design of TCDM, wherein each pair of data serves as a template for the other by turns. Specifically, as shown in Fig. 2,  $A@B$  and  $B@A$  represent that using  $d_A$  as the template pair to generate  $I_B$  and using  $d_B$  as the template pair to generate  $I_A$ , respectively. Using bidirectional training strategy, we derive the final loss function of TCDM as expressed:

$$\mathcal{L}_{TCDM} = \mathcal{L}_{DM_{A@B}} + \mathcal{L}_{DM_{B@A}}. \quad (4)$$

By integrating template-guided conditioning through bidirectional training strategies, we generate  $(N^{tr})^2$  training sample pairs solely based on  $N^{tr}$  image-mask pairs through random sampling and combinations, which significantly reduces the amount of data required for training the generator compared to previous methods[7, 10].

### 3.1.3. Training-free Mask Generation Module

Having more diverse masks indicates more morphologically heterogeneous images to be generated. To produce numerous masks that meet the stringent structural requirements of cardiac imaging, as shown in Fig. 3, our designed MGM employs a training-free strategy rather than training an additional generative network.

In inference stage, we select a small subset  $\mathbf{Temp} = \{\mathbf{d}_l^T\}_{l=1}^{N^T}$  from the test dataset  $\mathbf{D}^{ts} = \{\mathbf{d}_l^{ts}\}_{l=1}^{N^{ts}}$  to create a template library that provides random template pair for subsequent inference. We randomly choose a mask  $\mathbf{M}$  from  $\mathbf{Temp}$  and obtain fine-grained mask. Then,  $\mathbf{M}$  undergo an affine transformation and a non-rigid deformation to generate the registration filed matrix  $\Omega$  and the deformed coordinates  $\Psi$  as shown in Eq. (5):

$$\Omega, \Psi = \mathcal{T}_{nr}(\mathcal{T}_a(\mathbf{M}, \phi, \gamma, \varphi, \delta), \alpha, \zeta), \quad (5)$$

where  $\phi, \gamma, \varphi$ , and  $\delta$  control the affine transformation  $\mathcal{T}_a$ , as well as  $\alpha$  and  $\zeta$  regulate the non-rigid deformation  $\mathcal{T}_{nr}$ .

The discretization of voxel coordinates caused by deformation results in spatially disconnected micro-fractures in the deformed masks, thereby compromising the inherent spatial coherence of masks. This discontinuity adversely affects subsequent image generation tasks, particularly in preserving the integrity of coronary artery. To address this challenge, we utilize a max-pooling operator with a kernel size of  $2 \times 2 \times 2$  to perform morphological closing on each class of deformed mask, achieving the continuous mask  $\widetilde{\mathbf{M}}$ :

$$\widetilde{\mathbf{M}} = \bigcup_{i=1}^8 \text{Maxpool}_{2 \times 2 \times 2}(\Lambda(\mathbf{M}^i, \Omega, \Psi)), \quad (6)$$

where  $\Lambda$  represents the deformation function, and  $\mathbf{M}^i$  denotes the portion of  $\mathbf{M}$  that includes only the  $i^{\text{th}}$  class mask.

MGM supplies TCDM with a substantial collection of masks satisfying both topological consistency and diversity requirements, enabling the generation of large-scale synthetic datasets for downstream pre-training tasks.

## 3.2. Confidence-aware Adaptive Learning

As shown in Eq. (2), diffusion models are based on Hidden Markov Chains and sampling at each step is contingent upon the current state[15]. As shown in Fig. 2, we incorporate the SSV estimation during the reverse sampling process to obtain a **Confidence Map**, which represents the reliability of the synthetic images and are designed for our proposed downstream segmentation pre-training strategy.

### 3.2.1. Skip-Sampling Variance Estimation

Throughout the T-step reverse diffusion, once the model has sufficiently learned the distribution of a certain region, the sampling process for that region tends to be stable, leading to smaller variations across different steps. In contrast, for regions where the model has not yet achieved robust

learning, the reverse sampling process exhibits greater uncertainty, leading to the fluctuations in these uncertain areas.

According to the above analysis, we design the SSV estimation in consideration of the efficiency of diffusion model. Specifically, SSV takes  $k$ -step as intervals to perform staggered sampling over the  $T$ -step denoising process, resulting in  $T' = \{t_0, t_k, t_{2k}, \dots, t_{rk}\}$ , where  $r \cdot k \leq T - 1$ . For each  $t \in T'$ , we obtain the latent space feature  $\widetilde{\mathbf{Z}}_t$  and decode it to generate  $\widetilde{\mathbf{I}}_t$ . Consequently, we can derive a set of intermediate images represented by  $\Pi = \{\widetilde{\mathbf{I}}_{t_0}, \widetilde{\mathbf{I}}_{t_k}, \widetilde{\mathbf{I}}_{t_{2k}}, \dots, \widetilde{\mathbf{I}}_{t_{rk}}\}$ . Then we generate a confidence map  $\mathbf{CM}$  as follows:

$$\mathbf{CM} = \text{Norm}\left(\frac{\sum_{i=0}^r (\widetilde{\mathbf{I}}_{t_{ik}} - \overline{\Pi})}{r}\right), \quad (7)$$

where  $\overline{\Pi}$  denotes the average value of the image set  $\Pi$ , and the function  $\text{Norm}(\cdot)$  represents the normalization of the content. As  $\mathbf{CM}$  indicates the stability of the generation process and the certainty of synthetic images, the higher value means the stable generation process, implying higher confidence. Contrarily, lower values of  $\mathbf{CM}$  correspond to fluctuated generation resulting in lower reliability.

### 3.2.2. Using Confidence Map to Enhance Pre-training

For mask  $\mathbb{M}$  (either directly providing  $\mathbf{M}$  or deriving  $\widetilde{\mathbf{M}}$  from MGM), we synthesize its corresponding image  $\widetilde{\mathbf{I}}$  and confidence map  $\mathbf{CM}$  through TCDM and SSV, thereby forming a synthetic dataset entry  $\mathbf{d}_{syn} = \{\mathbb{M}, \widetilde{\mathbf{I}}, \mathbf{CM}\}$ . Most prior ‘‘synthesis then pre-training’’ approaches, as shown in Eq. (8), directly calculate the gradient for the each voxel without differentiation, where  $F$  refers to the downstream model and  $\mathcal{L}_{ori}$  denotes the original loss function.

$$\mathcal{L}_{ori} = \mathcal{L}(F(\widetilde{\mathbf{I}}), \mathbb{M}), \quad (8)$$

In contrast, our proposed CAL leverages the generated confidence map to promote the downstream segmentation pre-training according to Eq. (9), which dynamically adjusts the contribution of each voxel during the loss computation:

$$\mathcal{L}_{CAL} = \mathbf{CM} \cdot \mathcal{L}(F(\widetilde{\mathbf{I}}), \mathbb{M}). \quad (9)$$

In this way, CAL assigns higher weights to regions with higher confidence, thereby avoiding the interference of uncertain regions and achieving a more precise training effect.

## 4. Experiments

In this section, we first introduce the datasets, evaluation metrics, and setup for experiments. Subsequently, we compare our method with prior works through both quantitative and qualitative evaluations in image generation and downstream segmentation pre-training tasks. Finally, ablation studies are performed to confirm the effectiveness of each proposed components. Detailed information and additional results are provided in the supplementary material.

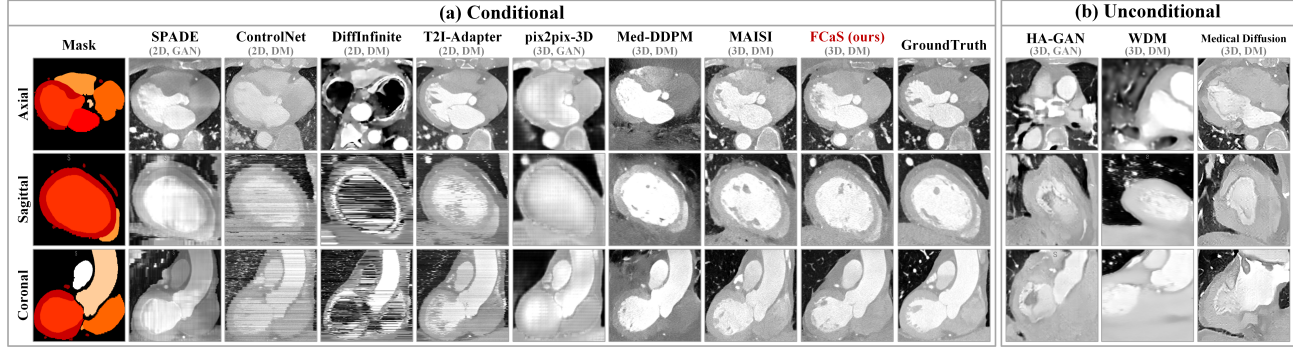


Figure 4. Comparison of synthetic fine-grained cardiac images generated by existing methods and our FCaS framework. (a) The results of the conditional generation methods based on the given mask. (b) The results of the unconditional generation methods.

Methods		Dim	Type	SSIM $\uparrow$	RMSE $\downarrow$	LPIPS $\downarrow$	FID $\downarrow$
Unconditional	HA-GAN[42]	3D	GAN	-	-	-	6.3975
	WDM[8]	3D	DM	-	-	-	5.2148
	Medical Diffusion[24]	3D	DM	-	-	-	7.1284
With Surroundings	SPADE[36]	2D	GAN	0.8442 $\pm$ 0.0152	0.1812 $\pm$ 0.0364	0.0855 $\pm$ 0.0512	2.9331
	ControlNet[55]	2D	DM	0.8739 $\pm$ 0.0197	0.1182 $\pm$ 0.0436	0.0685 $\pm$ 0.0324	2.0073
	T2I-Adapter[32]	2D	DM	0.8641 $\pm$ 0.0204	0.1272 $\pm$ 0.0488	<u>0.0621<math>\pm</math>0.0300</u>	<u>1.9812</u>
	DiffInfinite[1]	2D	DM	0.4076 $\pm$ 0.0368	0.6984 $\pm$ 0.3289	0.5943 $\pm$ 0.3725	7.4952
	pix2pix-3D[20]	3D	GAN	0.7499 $\pm$ 0.0263	0.3706 $\pm$ 0.1043	0.1366 $\pm$ 0.0821	3.9607
	Med-DDPM[7]	3D	DM	0.8561 $\pm$ 0.0153	0.2437 $\pm$ 0.0844	0.1038 $\pm$ 0.0549	3.2129
	MAISI[10]	3D	DM	0.9110 $\pm$ 0.0158	0.0836 $\pm$ 0.0141	0.0553 $\pm$ 0.0152	1.6881
W/o Surroundings	SPADE[36]	2D	GAN	0.8233 $\pm$ 0.0161	0.2283 $\pm$ 0.0764	0.1045 $\pm$ 0.0528	3.7782
	ControlNet[55]	2D	DM	0.8342 $\pm$ 0.0231	0.1975 $\pm$ 0.0683	0.0767 $\pm$ 0.0282	2.3926
	T2I-Adapter[32]	2D	DM	0.8424 $\pm$ 0.0281	0.2099 $\pm$ 0.0692	0.0724 $\pm$ 0.0324	2.4233
	DiffInfinite[1]	2D	DM	0.3874 $\pm$ 0.0392	0.7098 $\pm$ 0.3675	0.6039 $\pm$ 0.4317	7.8165
	pix2pix-3D[20]	3D	GAN	0.7272 $\pm$ 0.0272	0.3921 $\pm$ 0.1275	0.1458 $\pm$ 0.0983	4.1224
	Med-DDPM[7]	3D	DM	0.8128 $\pm$ 0.0168	0.3026 $\pm$ 0.0817	0.1284 $\pm$ 0.0893	3.7139
	MAISI[10]	3D	DM	0.9072 $\pm$ 0.0196	0.0954 $\pm$ 0.0181	0.0572 $\pm$ 0.0231	1.8214
	<b>FCaS (ours)</b>	3D	DM	<b>0.9243<math>\pm</math>0.0165</b>	<b>0.0731<math>\pm</math>0.0155</b>	<b>0.0541<math>\pm</math>0.0140</b>	<b>1.5821</b>

Table 1. Comparison with state-of-the-art methods in terms of generative evaluation metrics. **Bold** denotes the best results, and Underlined denotes the best results among 2D generative methods. “-” denotes the metrics is unavailable for this method.

## 4.1. Experiments Configurations

### 4.1.1. Dataset

**Generation stage.** We train generation model at this stage based on the ImageCAS[53], which is a large-scale coronary artery segmentation dataset that comprises 1000 cases. We partition the dataset into 200 cases for training and 800 cases for testing. Among the test set, 50 cases are placed into the template library, while the remaining 750 cases are used as references. All images undergo initial segmentation using pretrained nnU-Net[19] and TotalSegmentator[49] to generate masks for seven cardiac substructures and surrounding anatomical tissues, respectively.

**Pre-training stage.** For the downstream segmentation tasks, we select four public datasets and one private dataset, which focus on cardiac structural segmentation. Each dataset is split into training and testing sets at a ratio of 1:4. The four public datasets are ImageCHD[50], ImageALCAPA[52], ASOCA[9], and MM-WHS[57], respectively. The private dataset comprises 288 cases that include masks for coronary arteries and cardiac substructures.

### 4.1.2. Implementation Details

Our experiments compare with a series of representative methods, including unconditional and conditional methods applied in 2D and 3D spaces. We follow the setup of recent work[10] and utilize the MONAI framework[11] for the implementation of our method. In the generation stage, FCaS model is trained using the AdamW optimizer with an initial learning rate of  $1e^{-5}$  for a total of 200 epochs. Meanwhile, all data undergo resampling and are randomly cropped to a size of  $512 \times 512 \times 128$ , with a batch size of 4. During the inference phase, a sliding window of  $64 \times 64 \times 128$  is applied to recover latent features, outputting a 3D volume with a resolution of  $512 \times 512 \times 256$ . Additionally, FCaS is trained on a single NVIDIA RTX A100 GPU, while inference is performed on a single NVIDIA RTX 4090 GPU.

In the pre-training stage, all downstream segmentation experiments are performed on a single NVIDIA RTX 4090 GPU, and all data are processed according to the default preprocessing procedures of nnU-Net[19] and MedSAM[31]. The “Real-Only” experiments are trained on limited real data for 1000 epochs, while other methods

Method		Dim	ImageALCAPA[52]		ImageCHD[50]		MM-WHS[57] (7S)		ASOCA[9]	
			Dice (%) $\uparrow$	RDice (%) $\uparrow$						
nnU-Net	Real-Only	-	62.35 $\pm$ 8.76	66.14 $\pm$ 9.76	75.17 $\pm$ 8.83	79.34 $\pm$ 9.94	78.63 $\pm$ 2.42	80.88 $\pm$ 2.58	70.29 $\pm$ 8.37	74.58 $\pm$ 9.42
	SPADE [36]	2D	60.12 $\pm$ 10.37	64.43 $\pm$ 12.54	76.85 $\pm$ 9.31	79.98 $\pm$ 10.53	82.44 $\pm$ 2.87	85.73 $\pm$ 2.92	64.67 $\pm$ 10.15	68.93 $\pm$ 11.21
	ControlNet [55]	2D	61.38 $\pm$ 9.72	66.84 $\pm$ 9.61	<u>78.09<math>\pm</math>8.42</u>	<u>81.23<math>\pm</math>9.52</u>	85.17 $\pm$ 2.93	88.39 $\pm$ 3.01	<u>78.21<math>\pm</math>8.19</u>	<u>82.42<math>\pm</math>9.38</u>
	T2I-Adapter [32]	2D	62.61 $\pm$ 8.52	67.02 $\pm$ 9.43	77.58 $\pm$ 8.63	80.74 $\pm$ 9.74	86.22 $\pm$ 2.75	89.40 $\pm$ 2.87	77.83 $\pm$ 8.03	81.98 $\pm$ 9.12
	DiffInfinite [1]	2D	50.41 $\pm$ 18.62	54.53 $\pm$ 20.74	65.08 $\pm$ 15.17	69.32 $\pm$ 17.24	72.05 $\pm$ 6.84	75.23 $\pm$ 6.90	48.03 $\pm$ 18.62	52.22 $\pm$ 20.78
	pix2pix-3D [20]	3D	56.89 $\pm$ 12.51	61.02 $\pm$ 13.66	68.31 $\pm$ 13.32	72.52 $\pm$ 14.43	72.61 $\pm$ 7.46	75.79 $\pm$ 7.54	57.65 $\pm$ 15.63	61.82 $\pm$ 16.73
	Med-DDPM [7]	3D	62.87 $\pm$ 8.29	65.52 $\pm$ 10.82	74.29 $\pm$ 8.03	78.46 $\pm$ 9.11	86.37 $\pm$ 2.79	89.53 $\pm$ 2.87	75.53 $\pm$ 11.72	79.70 $\pm$ 12.88
	MAISI [10]	3D	63.42 $\pm$ 8.11	67.58 $\pm$ 9.22	78.79 $\pm$ 7.76	81.93 $\pm$ 8.86	88.51 $\pm$ 2.57	91.68 $\pm$ 2.64	81.22 $\pm$ 8.63	85.39 $\pm$ 9.75
	FCaS (ours)	3D	<b>64.09<math>\pm</math>8.31</b>	<b>68.26<math>\pm</math>9.43</b>	<b>79.05<math>\pm</math>7.83</b>	<b>82.21<math>\pm</math>8.97</b>	<b>89.31<math>\pm</math>2.76</b>	<b>92.48<math>\pm</math>2.83</b>	<b>82.23<math>\pm</math>7.85</b>	<b>86.41<math>\pm</math>8.91</b>
MedSAM	Real-Only	-	58.49 $\pm$ 3.72	62.76 $\pm$ 4.07	66.21 $\pm$ 5.83	70.39 $\pm$ 6.41	74.76 $\pm$ 5.87	77.98 $\pm$ 6.37	67.32 $\pm$ 11.42	71.48 $\pm$ 12.70
	SPADE [36]	2D	56.15 $\pm$ 5.69	60.32 $\pm$ 6.42	65.63 $\pm$ 7.85	69.78 $\pm$ 8.72	73.28 $\pm$ 6.29	76.45 $\pm$ 6.71	61.62 $\pm$ 15.08	65.79 $\pm$ 16.33
	ControlNet [55]	2D	59.58 $\pm$ 2.75	63.73 $\pm$ 2.97	71.07 $\pm$ 5.06	75.22 $\pm$ 5.58	76.29 $\pm$ 2.58	79.43 $\pm$ 2.74	70.12 $\pm$ 10.54	74.27 $\pm$ 11.51
	T2I-Adapter [32]	2D	<u>60.07<math>\pm</math>2.76</u>	<u>64.21<math>\pm</math>3.02</u>	<u>71.33<math>\pm</math>5.35</u>	<u>75.42<math>\pm</math>5.90</u>	<u>76.61<math>\pm</math>2.39</u>	<u>79.75<math>\pm</math>2.56</u>	69.77 $\pm$ 10.03	73.94 $\pm$ 11.08
	DiffInfinite [1]	2D	50.12 $\pm$ 9.43	54.27 $\pm$ 10.34	56.14 $\pm$ 15.72	60.31 $\pm$ 17.38	60.27 $\pm$ 11.09	63.44 $\pm$ 11.83	50.83 $\pm$ 17.85	53.99 $\pm$ 19.73
	pix2pix-3D [20]	3D	53.31 $\pm$ 7.76	57.48 $\pm$ 8.51	59.72 $\pm$ 13.18	63.87 $\pm$ 14.49	67.35 $\pm$ 8.87	70.49 $\pm$ 9.53	58.41 $\pm$ 17.06	62.55 $\pm$ 18.62
	Med-DDPM [7]	3D	58.17 $\pm$ 3.15	62.31 $\pm$ 3.48	68.79 $\pm$ 6.87	72.93 $\pm$ 7.65	74.93 $\pm$ 3.41	79.08 $\pm$ 3.57	65.87 $\pm$ 13.75	70.01 $\pm$ 14.92
	MAISI [10]	3D	59.71 $\pm$ 2.68	63.86 $\pm$ 2.95	71.42 $\pm$ 5.24	75.55 $\pm$ 5.82	77.38 $\pm$ 2.13	80.51 $\pm$ 2.22	70.51 $\pm$ 10.76	74.65 $\pm$ 11.85
	FCaS (ours)	3D	<b>60.63<math>\pm</math>2.65</b>	<b>64.80<math>\pm</math>2.89</b>	<b>71.92<math>\pm</math>4.97</b>	<b>76.05<math>\pm</math>5.51</b>	<b>78.75<math>\pm</math>1.29</b>	<b>81.89<math>\pm</math>1.33</b>	<b>71.83<math>\pm</math>9.73</b>	<b>76.01<math>\pm</math>10.71</b>

Table 2. Comparison of different methods in terms of pre-training performance on downstream segmentation tasks. **Bold** denotes the best results, and Underlined denotes the best results among 2D generative methods.

train on synthetic datasets for 800 epochs first, followed by fine-tuning on limited real data for 200 epochs.

#### 4.1.3. Evaluation Metrics

During the generation stage, we evaluate image quality using four metrics[10]: Structural Similarity Index (SSIM), Root Mean Square Error (RMSE), Fréchet Inception Distance (FID), and Learned Perceptual Image Patch Similarity (LPIPS). Specifically, SSIM, RMSE, and LPIPS are computed separately for each real image and synthesized image pair under the same mask, while FID is calculated between the entire sets of real and synthesized images to assess the global distribution distance. Since the unconditional methods do not include masks, only FID metric is applicable to these methods. In the downstream segmentation tasks, we use Dice and RDice [38] as our metrics.

## 4.2. Generation Comparison

During the generation and pre-training stages, we employ a shared set of 750 distinct reference masks from the test set of ImageCAS for all conditional methods. To ensure fair comparisons, FCaS does not include MGM for generating extra masks. In the ablation studies, we obtain numerous and diverse masks through MGM to validate the impact of synthesized data quantity on pre-training quality.

### 4.2.1. Qualitative Evaluation

Figure 4 presents a qualitative comparison between our FCaS and others. As shown, cardiac images generated by unconditional methods exhibit compromised topological consistency due to the lack of spatial guidance, whereas images produced by most conditional methods demonstrate preserved structural accuracy. Thus, the semantic guidance utilized in synthesis proves to be effective.

Meanwhile, for a given 3D fine-grained mask, 2D-based methods process each axial slice independently, whereas

Group	Real	Syn	Part A		Part B	
			Dice (%) $\uparrow$	RDice (%) $\uparrow$	Dice (%) $\uparrow$	RDice (%) $\uparrow$
I	176	0	88.43 $\pm$ 11.32	92.10 $\pm$ 12.68	78.89 $\pm$ 11.83	83.32 $\pm$ 13.04
II	20	0	86.04 $\pm$ 13.24	89.84 $\pm$ 9.63	72.37 $\pm$ 13.49	79.54 $\pm$ 12.81
III	20	400	88.62 $\pm$ 12.57	91.75 $\pm$ 9.79	78.91 $\pm$ 11.39	83.23 $\pm$ 12.76
IV	20	1000	<b>89.68<math>\pm</math>11.92</b>	<b>92.68<math>\pm</math>10.44</b>	<b>80.29<math>\pm</math>10.94</b>	<b>84.38<math>\pm</math>12.20</b>

Table 3. Impact of FCaS-synthesized images on downstream segmentation tasks under data scarcity. Part A - Seven heart substructures defined by MM-WHS[57]. Part B - Coronary arteries.

3D-based methods holistically process and generate coherent 3D volumes. Consequently, as illustrated in Figure 4(a), sagittal and coronal visualizations reveal that images generated by SPADE, ControlNet, and T2I-Adapter exhibit noticeable discontinuities, whereas 3D-based methods demonstrate superior spatial coherence. Additionally, DiffInfinite process the guidance information from each category separately, which inherently lacks inter-class correlations, causing significant intensity biases in its outputs. In contrast, 3D methods show better performance compared to 2D approaches. Most existing methods primarily converge on large organs while exhibiting poor performance on fine structural details. Meanwhile, although MAISI achieves satisfactory cardiac structure, it still exhibits intensity inaccuracy on small fine-grained details, which results in the inferior performance to our FCaS in down-stream pre-training. Through using template-guided condition, our FCaS enables the generation of images with enhanced topological consistency while achieving superior visualization in fine structural details. Furthermore, we invite two clinically experienced experts to evaluate and rank the synthesized data generated by various methods. Consequently, our proposed FCaS achieves superior rankings and outstanding average scores, thereby highlighting the practical applicability of our methods in clinical scenarios.

### 4.2.2. Quantitative Evaluation

As shown in Tab. 1, our proposed FCaS achieves state-of-the-art performance on fine-grained cardiac image synthesis, which demonstrates best structural fidelity and semantic representation comparable to real cardiac images. Generally speaking, most conditional methods demonstrate superior performance over unconditional methods. Although ControlNet and T2I-Adapter are 2D-based models, their integration with powerful generative capacity of diffusion models enables satisfactory performance with surrounding tissues. Moreover, SPADE exhibits minimal structural bias but significant intensity discrepancies, leading to relatively high SSIM and low RMSE. Meanwhile, MAISI employs 3D diffusion models for feature representation, achieving remarkable performance across four evaluation metrics. Notably, as shown in “with surroundings” and “w/o surroundings” parts in Tab. 1, the significant degradation is observed across all the methods when the masks of surrounding tissues are removed from the reference. However, our FCaS still produces outstanding results even in the absence of surrounding tissues. We attribute the robustness to the template-guided conditioning, which provides structural constraints for the generation process.

### 4.3. Downstream Segmentation Pre-training

We evaluate the effectiveness of synthetic images in facilitating data-driven segmentation tasks, particularly where high-quality training data is scarce. As shown in Tab. 2, the “Real-Only” baseline refers to the direct segmentation performance using limited real data samples without any pre-training. Other compared methods only take images as input and employ masks for supervision, while our FCaS additionally introduces confidence maps to dynamically adjust the voxel-wise contributions of synthesized images to the supervision loss. For most methods, utilizing synthetic images for pre-training demonstrate Dice improvement when real data is scarce. As listed in Tab. 2, pre-training with our FCaS-generated images combined with the CAL strategy achieves the best performance enhancement across all tasks for both nnU-Net and MedSAM.

Specifically, when using nnU-Net, FCaS attains noticeable Dice improvements of 1.74%, 3.88%, 10.68%, and 11.94% across the four datasets, respectively. Also, FCaS helps MedSAM achieve notable gains of 2.14%, 5.71%, 3.99%, and 4.51%. Synthetic images of most methods exhibit Dice improvements, except for DiffInfinite and pix2pix-3D. Notably, MedSAM is a 2D segmentation framework and has higher tolerance for inter-slice discontinuity. Therefore, images generated by 2D-based methods could achieve comparable results with ours on MedSAM.

Direction		Condition		SSV	FID↓	LPIPS↓	Avg Dice (%) ↑
One	Bi	Norm	Temp				
✓		✓			2.4239	0.0842±0.0282	83.97±13.48
	✓	✓			2.3907	0.0811±0.0265	84.21±13.24
✓			✓		1.6230	0.0673±0.0194	85.65±12.00
	✓		✓		<b>1.5821</b>	<b>0.0541±0.0140</b>	86.05±11.65
	✓		✓	✓	<b>1.5821</b>	<b>0.0541±0.0140</b>	<b>87.27±10.31</b>

Table 4. Ablation study of different components in FCaS framework. Notably, “One” and “Bi” denote the presence or absence of a bidirectional training strategy in the TCDM, while “Norm” refers to applying mask normalization alone and “Temp” indicates the proposed template-guided condition.

### 4.4. Ablation Study and Model Analysis

To investigate the specific impacts of FCaS on downstream pre-training and explain the roles of its main modules, we conduct several experiments using nnU-Net[19] on our private cardiac dataset containing 288 cases. The whole private dataset is split into two parts, where Part A contains seven cardiac substructures as defined by MM-WHS[57], and Part B contains the main branches of coronary arteries. On the one hand, we explore the critical role of our MGM by adjusting the ratio between synthetic data and real data during pre-training and fine-tuning phases, respectively. Specifically, we utilize 50 templates from template library of ImageCAS, employing the MGM to generate abundant references for image synthesis. As shown in Tab. 3, groups I and II exhibit significant performance degradation when training data is substantially reduced, particularly for coronary arteries. When we introduce synthetic data for pre-training followed by fine-tuning with limited real images, nnU-Net exhibits recovery of segmentation accuracy. This two-stage process achieves remarkable improvements, and the Dice of group III increases by 2.58% and 6.54% for Part A and Part B, respectively, compared to group II. As the quantity of synthetic data progressively increases (group IV), nnU-Net shows continuous improvement in performance. With numerous and diverse masks generated by MGM, TCDM can further synthesize sufficient images satisfying both topological consistency and morphological heterogeneity to fulfill downstream pre-training demands, thereby demonstrating MGM’s indispensable role.

On the other hand, we conduct an ablation study to evaluate the effectiveness of bidirectional training strategy, template condition, and SSV, respectively. Notably, FID and LPIPS are utilized to assess the generation quality, while Avg Dice measures the impact of pre-training on downstream segmentation tasks based on the synthesized image. The results, listed in Table 4, demonstrate that all proposed components significantly enhance performance. Specifically, since SSV is only applied during the pre-training stage, it does not influence the image generation metrics but substantially improves the accuracy of downstream pre-training on segmentation task.

## 5. Conclusion

In this work, we present a framework FCaS to address the scarcity of annotated cardiac images. To our best knowledge, FCaS is the first work that aims to generate fine-grained and high-quality cardiac images with topological details preserved. To achieve this goal, we propose a 3D Template-guided Conditional Diffusion Model (TCDM) that guides reverse diffusion process using template conditions with reference masks to provide fine-grained spatial information, leading to high-quality images. Meanwhile, we introduce the Mask Generation Module (MGM) to obtain numerous reference masks ensuring topological consistency, which facilitates the diverse generation. Furthermore, our Confidence-aware Adaptive Learning (CAL) strategy dynamically adjusts the contribution of each voxel in calculating loss function, which addresses uncertain regions in the synthesized images. Experimental results demonstrate that the superior performance of FCaS in generating high-quality cardiac images and enhancing downstream segmentation tasks, showing its substantial potential in advancing cardiac medical imaging analysis.

## References

- [1] Marco Aversa, Gabriel Nobis, Miriam Hägele, Kai Standvoss, Mihaela Chirica, Roderick Murray-Smith, Ahmed M Alaa, Lukas Ruff, Daniela Ivanova, Wojciech Samek, et al. Diffinfinite: Large mask-image synthesis via parallel random patch diffusion in histopathology. *Advances in Neural Information Processing Systems*, 36:78126–78141, 2023. 1, 2, 3, 6, 7
- [2] Tariq Berrada, Jakob Verbeek, Camille Couprie, and Kartheek Alahari. Unlocking pre-trained image backbones for semantic image synthesis. In *In Proceedings of IEEE International Conference on Computer Vision and Pattern Recognition*, pages 7840–7849. IEEE, 2024. 3
- [3] Bing Cao, Han Zhang, Nannan Wang, Xinbo Gao, and Dinggang Shen. Auto-gan: self-supervised collaborative learning for medical image synthesis. In *Proceedings of the AAAI conference on artificial intelligence*, pages 10486–10493, 2020. 2
- [4] Qi Chen, Xiaoxi Chen, Haorui Song, Zhiwei Xiong, Alan Yuille, Chen Wei, and Zongwei Zhou. Towards generalizable tumor synthesis. In *In Proceedings of IEEE International Conference on Computer Vision and Pattern Recognition*, pages 11147–11158, 2024. 3
- [5] Onat Dalmaz, Mahmut Yurt, and Tolga Çukur. Resvit: residual vision transformers for multimodal medical image synthesis. *IEEE Transactions on Medical Imaging*, 41(10): 2598–2614, 2022. 2
- [6] Sanuwani Dayarathna, Kh Tohidul Islam, Sergio Uribe, Guang Yang, Munawar Hayat, and Zhaolin Chen. Deep learning based synthesis of mri, ct and pet: Review and analysis. *Medical image analysis*, 92:103046, 2024. 2
- [7] Zolnamar Dorjsembe, Hsing-Kuo Pao, Sodtavilan Odonchimed, and Furen Xiao. Conditional diffusion models for semantic 3d brain mri synthesis. *IEEE Journal of Biomedical and Health Informatics*, 2024. 2, 4, 6, 7
- [8] Paul Friedrich, Julia Wolleb, Florentin Bieder, Alicia Durrer, and Philippe C Cattin. Wdm: 3d wavelet diffusion models for high-resolution medical image synthesis. In *MIC-CAI Workshop on Deep Generative Models*, pages 11–21. Springer, 2024. 6, 2
- [9] Ramtin Gharlegghi, Dona Adikari, Katy Ellenberger, Sze-Yuan Ooi, Chris Ellis, Chung-Ming Chen, Ruochen Gao, Yuting He, Raabid Hussain, Chia-Yen Lee, Jun Li, Jun Ma, Ziwei Nie, Bruno Oliveira, Yaolei Qi, Youssef Skandarani, João L. Vilaça, Xiyue Wang, Sen Yang, Arcot Sowmya, and Susann Beier. Automated segmentation of normal and diseased coronary arteries – the asoca challenge. *Computerized Medical Imaging and Graphics*, 97:102049, 2022. 6, 7, 1
- [10] Pengfei Guo, Can Zhao, Dong Yang, Ziyue Xu, Vishwesh Nath, Yucheng Tang, Benjamin Simon, Mason Belue, Stephanie Harmon, Baris Turkbey, et al. Maisi: Medical ai for synthetic imaging. *arXiv preprint arXiv:2409.11169*, 2024. 2, 4, 6, 7
- [11] Vikash Gupta, Barbaros Erdal, Carolina Ramirez, Ralf Floca, Bradley Genereaux, Sidney Bryson, Christopher Bridge, Jens Kleesiek, Felix Nensa, Rickmer Braren, Khaled Younis, Tobias Penzkofer, Andreas Michael Bucher, Ming Melvin Qin, Gigon Bae, Hyeonhoon Lee, M Jorge Cardoso, Sebastien Ourselin, Eric Kerfoot, Rahul Choudhury, Richard D White, Tessa Cook, David Bericat, Matthew Lungren, Risto Haukioja, and Haris Shuaib. Current state of community-driven radiological ai deployment in medical imaging. *JMIR AI*, 3:e55833, 2024. 6
- [12] Kun Han, Yifeng Xiong, Chenyu You, Pooya Khosravi, Shanlin Sun, Xiangyi Yan, James S Duncan, and Xiaohui Xie. Medgen3d: A deep generative framework for paired 3d image and mask generation. In *International Conference on Medical Image Computing and Computer-Assisted Intervention*, pages 759–769. Springer, 2023. 3
- [13] Yuting He, Guanyu Yang, Rongjun Ge, Yang Chen, Jean-Louis Coatrieux, Boyu Wang, and Shuo Li. Geometric visual similarity learning in 3d medical image self-supervised pre-training. In *In Proceedings of IEEE International Conference on Computer Vision and Pattern Recognition*, pages 9538–9547, 2023. 2
- [14] Yuting He, Boyu Wang, Rongjun Ge, Yang Chen, Guanyu Yang, and Shuo Li. Homeomorphism prior for false positive and negative problem in medical image dense contrastive representation learning. *IEEE Transactions on Pattern Analysis and Machine Intelligence*, 2025. 2
- [15] Jonathan Ho, Ajay Jain, and Pieter Abbeel. Denoising diffusion probabilistic models. *Advances in neural information processing systems*, 33:6840–6851, 2020. 3, 5
- [16] Yutao Hu, Qixiong Wang, Wenqi Shao, Enze Xie, Zhenguo Li, Jungong Han, and Ping Luo. Beyond one-to-one: Rethinking the referring image segmentation. In *In Proc. of IEEE International Conference on Computer Vision*, pages 4067–4077, 2023. 2
- [17] Yutao Hu, Tianbin Li, Quanfeng Lu, Wenqi Shao, Junjun He, Yu Qiao, and Ping Luo. Omnimedvqa: A new large-scale

- comprehensive evaluation benchmark for medical lvlm. In *In Proceedings of IEEE International Conference on Computer Vision and Pattern Recognition*, pages 22170–22183, 2024. 2
- [18] Yawen Huang, Ling Shao, and Alejandro F Frangi. Simultaneous super-resolution and cross-modality synthesis of 3d medical images using weakly-supervised joint convolutional sparse coding. In *In Proceedings of IEEE International Conference on Computer Vision and Pattern Recognition*, pages 6070–6079, 2017. 3
- [19] Fabian Isensee, Paul F Jaeger, Simon AA Kohl, Jens Petersen, and Klaus H Maier-Hein. nnu-net: a self-configuring method for deep learning-based biomedical image segmentation. *Nature methods*, 18(2):203–211, 2021. 6, 8
- [20] Phillip Isola, Jun-Yan Zhu, Tinghui Zhou, and Alexei A Efros. Image-to-image translation with conditional adversarial networks. In *In Proceedings of IEEE International Conference on Computer Vision and Pattern Recognition*, pages 1125–1134, 2017. 1, 3, 6, 7
- [21] Jaebong Jeong, Janghun Jo, Sunghyun Cho, and Jaesik Park. 3d scene painting via semantic image synthesis. In *In Proceedings of IEEE International Conference on Computer Vision and Pattern Recognition*, pages 2262–2272, 2022. 3
- [22] Euijin Jung, Miguel Luna, and Sang Hyun Park. Conditional gan with an attention-based generator and a 3d discriminator for 3d medical image generation. In *International Conference on Medical Image Computing and Computer-Assisted Intervention*, pages 318–328. Springer, 2021. 2, 3
- [23] Sharif Amit Kamran, Khondker Fariha Hossain, Alireza Tavakkoli, Stewart Lee Zuckerbrod, and Salah A Baker. Vtgan: Semi-supervised retinal image synthesis and disease prediction using vision transformers. In *In Proc. of IEEE International Conference on Computer Vision*, pages 3235–3245, 2021. 4
- [24] Firas Khader, Gustav Müller-Franzes, Soroosh Tayebi Arasteh, Tianyu Han, Christoph Haarbuerger, Maximilian Schulze-Hagen, Philipp Schad, Sandy Engelhardt, Bettina Baeßler, Sebastian Foersch, et al. Denoising diffusion probabilistic models for 3d medical image generation. *Scientific Reports*, 13(1):7303, 2023. 4, 6, 2
- [25] Jonghun Kim and Hyunjin Park. Adaptive latent diffusion model for 3d medical image to image translation: Multimodal magnetic resonance imaging study. In *In Proceedings of IEEE Winter Conference on Applications of Computer Vision*, pages 7604–7613, 2024. 3
- [26] Subhadeep Koley, Ayan Kumar Bhunia, Deeptanshu Sekhri, Aneeshan Sain, Pinaki Nath Chowdhury, Tao Xiang, and Yi-Zhe Song. It’s all about your sketch: Democratizing sketch control in diffusion models. In *In Proceedings of IEEE International Conference on Computer Vision and Pattern Recognition*, pages 7204–7214, 2024. 3
- [27] Linus Kreitner, Johannes C Paetzold, Nikolaus Rauch, Chen Chen, Ahmed M Hagag, Alaa E Fayed, Sobha Sivaprasad, Sebastian Rausch, Julian Weichsel, Bjoern H Menze, et al. Synthetic optical coherence tomography angiographs for detailed retinal vessel segmentation without human annotations. *IEEE Transactions on Medical Imaging*, 43(6):2061–2073, 2024. 2, 4
- [28] Jin Liu, Huiyuan Fu, Xin Wang, and Huadong Ma. Swinit: Hierarchical image-to-image translation framework without cycle consistency. *IEEE Transactions on Circuits and Systems for Video Technology*, 34(7):5546–5559, 2024. 3
- [29] Zhengyao Lv, Yuxiang Wei, Wangmeng Zuo, and Kwan-Yee K Wong. Place: Adaptive layout-semantic fusion for semantic image synthesis. In *In Proceedings of IEEE International Conference on Computer Vision and Pattern Recognition*, pages 9264–9274, 2024. 3
- [30] Jinhao Lyu, Ying Fu, Mingliang Yang, Yongqin Xiong, Qi Duan, Caohui Duan, Xueyang Wang, Xinbo Xing, Dong Zhang, Jiaji Lin, et al. Generative adversarial network-based noncontrast ct angiography for aorta and carotid arteries. *Radiology*, 309(2):e230681, 2023. 3
- [31] Jun Ma, Yuting He, Feifei Li, Lin Han, Chenyu You, and Bo Wang. Segment anything in medical images. *Nature Communications*, 15(1):654, 2024. 6
- [32] Chong Mou, Xintao Wang, Liangbin Xie, Yanze Wu, Jian Zhang, Zhongang Qi, and Ying Shan. T2i-adapter: Learning adapters to dig out more controllable ability for text-to-image diffusion models. In *Proceedings of the AAAI conference on artificial intelligence*, pages 4296–4304, 2024. 3, 6, 7
- [33] Gustav Müller-Franzes, Jan Moritz Niehues, Firas Khader, Soroosh Tayebi Arasteh, Christoph Haarbuerger, Christiane Kuhl, Tianci Wang, Tianyu Han, Teresa Nolte, Sven Nebelung, et al. A multimodal comparison of latent denoising diffusion probabilistic models and generative adversarial networks for medical image synthesis. *Scientific Reports*, 13(1):12098, 2023. 3
- [34] Dong Nie, Roger Trullo, Jun Lian, Li Wang, Caroline Petitjean, Su Ruan, Qian Wang, and Dinggang Shen. Medical image synthesis with deep convolutional adversarial networks. *IEEE Transactions on Biomedical Engineering*, 65(12):2720–2730, 2018. 2
- [35] Richard Osuala, Smriti Joshi, Apostolia Tsirikoglou, Lidia Garrucho, Walter HL Pinaya, Oliver Diaz, and Karim Lekadir. Pre-to post-contrast breast mri synthesis for enhanced tumour segmentation. In *Medical Imaging 2024: Image Processing*, pages 226–237. SPIE, 2024. 3
- [36] Taesung Park, Ming-Yu Liu, Ting-Chun Wang, and Jun-Yan Zhu. Semantic image synthesis with spatially-adaptive normalization. In *In Proceedings of IEEE International Conference on Computer Vision and Pattern Recognition*, pages 2337–2346, 2019. 1, 3, 6, 7
- [37] Junbo Peng, Richard LJ Qiu, Jacob F Wynne, Chih-Wei Chang, Shaoyan Pan, Tonghe Wang, Justin Roper, Tian Liu, Pretesh R Patel, David S Yu, et al. Cbct-based synthetic ct image generation using conditional denoising diffusion probabilistic model. *Medical physics*, 51(3):1847–1859, 2024. 3
- [38] Yaolei Qi, Han Xu, Yuting He, Guanyu Li, Zehang Li, Youyong Kong, Jean-Louis Coatrieux, Huazhong Shu, Guanyu Yang, and Shengxian Tu. Examinee-examiner network: Weakly supervised accurate coronary lumen segmentation using centerline constraint. *IEEE Transactions on Image Processing*, 30:9429–9441, 2021. 2, 7
- [39] Yaolei Qi, Yuting He, Xiaoming Qi, Yuan Zhang, and Guanyu Yang. Dynamic snake convolution based on topo-

- logical geometric constraints for tubular structure segmentation. In *In Proc. of IEEE International Conference on Computer Vision*, pages 6070–6079, 2023. 2
- [40] Partho P Sengupta, Damini Dey, Rhodri H Davies, Nicolas Duchateau, and Naveena Yanamala. Challenges for augmenting intelligence in cardiac imaging. *The Lancet Digital Health*, 6(10):e739–e748, 2024. 2
- [41] Jiacheng Shi, Yuting He, Youyong Kong, Jean-Louis Coatrieux, Huazhong Shu, Guanyu Yang, and Shuo Li. Xmorpher: Full transformer for deformable medical image registration via cross attention. In *International Conference on Medical Image Computing and Computer-Assisted Intervention*, pages 217–226. Springer, 2022. 2
- [42] Li Sun, Junxiang Chen, Yanwu Xu, Mingming Gong, Ke Yu, and Kayhan Batmanghelich. Hierarchical amortized gan for 3d high resolution medical image synthesis. *IEEE Journal of Biomedical and Health Informatics*, 26(8):3966–3975, 2022. 6, 2
- [43] Zhentao Tan, Menglei Chai, Dongdong Chen, Jing Liao, Qi Chu, Bin Liu, Gang Hua, and Nenghai Yu. Diverse semantic image synthesis via probability distribution modeling. In *In Proceedings of IEEE International Conference on Computer Vision and Pattern Recognition*, pages 7962–7971, 2021. 3
- [44] Zhentao Tan, Dongdong Chen, Qi Chu, Menglei Chai, Jing Liao, Mingming He, Lu Yuan, Gang Hua, and Nenghai Yu. Efficient semantic image synthesis via class-adaptive normalization. *IEEE Transactions on Pattern Analysis and Machine Intelligence*, 44(9):4852–4866, 2021. 3
- [45] Haoshen Wang, Zhentao Liu, Kaicong Sun, Xiaodong Wang, Dinggang Shen, and Zhiming Cui. 3d meddiffusion: A 3d medical diffusion model for controllable and high-quality medical image generation. *arXiv preprint arXiv:2412.13059*, 2024. 2, 4
- [46] Jinzhuo Wang, Kai Wang, Yunfang Yu, Yuxing Lu, Wen-chao Xiao, Zhuo Sun, Fei Liu, Zixing Zou, Yuanxu Gao, Lei Yang, et al. Self-improving generative foundation model for synthetic medical image generation and clinical applications. *Nature Medicine*, pages 1–9, 2024. 4
- [47] Qixun Wang, Xu Bai, Haofan Wang, Zekui Qin, Anthony Chen, Huaxia Li, Xu Tang, and Yao Hu. Instantid: Zero-shot identity-preserving generation in seconds. *arXiv preprint arXiv:2401.07519*, 2024. 3
- [48] Yi Wang, Lu Qi, Ying-Cong Chen, Xiangyu Zhang, and Ji-aya Jia. Image synthesis via semantic composition. In *In Proc. of IEEE International Conference on Computer Vision*, pages 13749–13758, 2021. 3
- [49] Jakob Wasserthal, Hanns-Christian Breit, Manfred T Meyer, Maurice Pradella, Daniel Hinck, Alexander W Sauter, Tobias Heye, Daniel T Boll, Joshy Cyriac, Shan Yang, et al. Totalsegmentator: robust segmentation of 104 anatomic structures in ct images. *Radiology: Artificial Intelligence*, 5(5):e230024, 2023. 6
- [50] Xiaowei Xu, Tianchen Wang, Jian Zhuang, Haiyun Yuan, Meiping Huang, Jianzheng Cen, Qianjun Jia, Yuhao Dong, and Yiyu Shi. Imagechd: A 3d computed tomography image dataset for classification of congenital heart disease. In *International Conference on Medical Image Computing and Computer-Assisted Intervention*, pages 77–87. Springer, 2020. 6, 7, 1
- [51] Yanwu Xu, Li Sun, Wei Peng, Shuyue Jia, Katelyn Morrison, Adam Perer, Afroz Zandifar, Shyam Visweswaran, Motahhare Eslami, and Kayhan Batmanghelich. Medsyn: Text-guided anatomy-aware synthesis of high-fidelity 3d ct images. *IEEE Transactions on Medical Imaging*, 2024. 4
- [52] An Zeng, Chenxi Mi, Dan Pan, Qing Lu, and Xiaowei Xu. Imagealcapa: A 3d computed tomography image dataset for automatic segmentation of anomalous left coronary artery from pulmonary artery. In *2022 IEEE International Conference on Bioinformatics and Biomedicine (BIBM)*, pages 1800–1803. IEEE, 2022. 6, 7, 1
- [53] An Zeng, Chunbiao Wu, Guisen Lin, Wen Xie, Jin Hong, Meiping Huang, Jian Zhuang, Shanshan Bi, Dan Pan, Najeeb Ullah, et al. Imagecas: A large-scale dataset and benchmark for coronary artery segmentation based on computed tomography angiography images. *Computerized Medical Imaging and Graphics*, 109:102287, 2023. 6, 1, 2
- [54] Yu Zeng, Zhe Lin, Jianming Zhang, Qing Liu, John Collo-mosse, Jason Kuen, and Vishal M Patel. Scenecomposer: Any-level semantic image synthesis. In *In Proceedings of IEEE International Conference on Computer Vision and Pattern Recognition*, pages 22468–22478, 2023. 3
- [55] Lvmin Zhang, Anyi Rao, and Maneesh Agrawala. Adding conditional control to text-to-image diffusion models. In *In Proc. of IEEE International Conference on Computer Vision*, pages 3836–3847, 2023. 3, 6, 7
- [56] Amy Zhao, Guha Balakrishnan, Fredo Durand, John V Gut-tag, and Adrian V Dalca. Data augmentation using learned transformations for one-shot medical image segmentation. In *In Proceedings of IEEE International Conference on Computer Vision and Pattern Recognition*, pages 8543–8553, 2019. 2
- [57] Xiahai Zhuang. Multivariate mixture model for myocardial segmentation combining multi-source images. *IEEE Transactions on Pattern Analysis and Machine Intelligence*, 41(12):2933–2946, 2019. 6, 7, 8, 1

# FCaS: Fine-grained Cardiac Image Synthesis based on 3D Template Conditional Diffusion Model

## Supplementary Material

### 6. More Details of Dataset and Metrics

#### 6.1. Dataset

**ImageCAS**[53] is a large-scale coronary artery segmentation dataset consisting of 1,000 3D Computed Tomography Angiography (CTA) images. It includes data from 414 female and 586 male patients, with average ages of 59.98 years and 57.68 years, respectively. The dataset contains annotations for coronary arteries including the Left Main (LM), Left Anterior Descending (LAD), Left Circumflex (LCX), Right Coronary Artery (RCA), First Diagonal Branch (D1), Second Diagonal Branch (D2), Third Diagonal Branch (D3), First Obtuse Marginal Branch (OM1), Second Obtuse Marginal Branch (OM2), Third Obtuse Marginal Branch (OM3), Intermediate Branch (RI), Posterior Descending Artery (PDA), and Acute Marginal Branch (AM1), following the 17-segment nomenclature of the American Heart Association (AHA).

**ImageCHD**[50] contains 110 3D Computed Tomography (CT) images that represent various types of congenital heart disease (CHD). This dataset is relatively substantial compared to existing medical imaging datasets. The annotations include labels for the Left Ventricle (LV), Right Ventricle (RV), Left Atrium (LA), Right Atrium (RA), Myocardium (Myo), Aorta (Ao), and Pulmonary Artery (PA).

**ImageALCAPA**[52] consists of 30 3D CTA images collected using the SOMATOM Definition Flash CT machine. All images are preoperative CTA scans for ALCAPA (Anomalous Left Coronary Artery from the Pulmonary Artery) and include segmentation of multiple anatomical structures, such as Myocardium (Myo), Left Ventricle (LV), Right Ventricle (RV), Pulmonary Artery (PA), Aorta (Ao), Left Coronary Artery (LCA), and Right Coronary Artery (RCA).

**ASOCA**[9] includes a training set of 40 cardiac CTA (CCTA) images, which visualize the coronary arteries. It consists of data from 20 healthy patients and 20 patients diagnosed with coronary artery disease. The segmentation object includes the left and right coronary arteries, and their branching segments (Left Anterior Descending, Left Circumflex, Septal, Diagonal, Obtuse Marginal, and Ramus Intermedius if present).

**MM-WHS**[57] comprises a total of 120 multimodal cardiac images, including 60 cardiac CT/CTA and 60 cardiac MRI images. These images encompass the whole heart and its major substructures, all collected in a real clinical environment for clinical diagnostic purposes. The training set pro-

vides manual segmentation annotations for seven key cardiac substructures, including the Left Ventricle (LV), Right Ventricle (RV), Left Atrium (LA), Right Atrium (RA), Myocardium (Myo), Ascending Aorta (Ao), and Pulmonary Artery (PA).

#### 6.2. Metrics

**SSIM** (Structural Similarity Index) is an objective metric designed to comprehensively evaluate image quality based on three perceptual aspects: luminance, contrast, and structure. For a given mask  $M$ , the SSIM is computed using Eq. (10) between the generated image  $X$  and the corresponding ground truth image  $Y$ . The SSIM ranges from 0 to 1, where higher values indicate greater similarity between  $X$  and  $Y$ .

$$\text{SSIM}(X, Y) = \frac{(2\mu_X\mu_Y + C_1)(2\sigma_{XY}^2 + C_2)}{(\mu_X^2 + \mu_Y^2 + C_1)(\sigma_X^2 + \sigma_Y^2 + C_2)}, \quad (10)$$

where  $\mu_X$  and  $\mu_Y$  denote the mean values of  $X$  and  $Y$ , respectively.  $\sigma_{XY}^2$ ,  $\sigma_X^2$ , and  $\sigma_Y^2$  represent the covariance between  $X$  and  $Y$ , and the variance of  $X$  and  $Y$ , respectively.

**RMSE** (Root Mean Square Error) is a commonly used statistical metric for measuring the differences between predicted values and ground truth values. A smaller RMSE indicates a smaller discrepancy between the two. The formula for calculating RMSE is given as follows, where  $h$ ,  $w$ , and  $d$  represent the dimensions of the image:

$$\text{RMSE}(X, Y) = \sqrt{\frac{1}{h \cdot w \cdot d} \sum_{i=1}^h \sum_{j=1}^w \sum_{k=1}^d (X_{i,j,k} - Y_{i,j,k})^2}. \quad (11)$$

**FID** (Fréchet Inception Distance) is a metric used to assess the quality of generated images by measuring the difference in feature distributions between images. A smaller FID value indicates a smaller distributional difference between the two image sets. The formula is as follows:

$$\text{FID}(X, Y) = \|\mu_r - \mu_g\|^2 + \text{Tr} \left( \Sigma_r + \Sigma_g - 2(\Sigma_r \Sigma_g)^{\frac{1}{2}} \right), \quad (12)$$

where,  $\text{Tr}$  denotes the trace of a matrix, while  $\mu$  and  $\Sigma$  represent the mean and covariance of the features, respectively.  $X$  and  $Y$  denote the sets of generated images and ground truth images, while  $r$  and  $g$  refer to the features of these two data types.

**LPIPS** (Learned Perceptual Image Patch Similarity) is a metric designed to evaluate the perceptual similarity between images. By mimicking the human visual system, it

measures the perceptual differences between images. The formula for computing LPIPS is as follows:

$$\text{LPIPS}(\mathbf{X}, \mathbf{Y}) = \sum_{i=1}^L w_i \cdot \frac{1}{N_i} \|f_i(\mathbf{X}) - f_i(\mathbf{Y})\|_2^2, \quad (13)$$

where  $f_i$  represents the  $i^{\text{th}}$  layer of the feature extraction network, and  $N_i$  denotes the number of elements in the features extracted from that layer.  $w_i$  refers to the learned weight associated with the  $i^{\text{th}}$  layer.

**Dice** (Dice Coefficient) is used to measure the similarity between two sets and is widely applied in image segmentation. Given an input image  $I$  and its corresponding ground truth mask  $Q$ , the segmentation model outputs a predicted mask  $P$ . The Dice is calculated as follows:

$$\text{Dice}(\mathbf{P}, \mathbf{Q}) = \frac{2|\mathbf{P} \cap \mathbf{Q}|}{|\mathbf{P}| + |\mathbf{Q}|}. \quad (14)$$

**RDice** (Relative Dice Coefficient) is a variant of the conventional Dice Coefficient, which improves the robustness of segmentation of small and fine objects. The ground truth  $Q$  undergoes morphological dilation to obtain  $Q'$ . Subsequently, the intersection of  $Q'$  and the predicted segmentation  $P$  is computed to yield  $P'$ . The RDice is then calculated as follows:

$$\text{RDice}(\mathbf{P}, \mathbf{Q}) = \frac{2|\mathbf{P}' \cap \mathbf{Q}|}{|\mathbf{P}'| + |\mathbf{Q}|}, \quad (15)$$

## 7. More Visualization Results

### 7.1. Synthetic Images of FCaS

As shown in Fig. 5, we present additional FCaS-synthesized cardiac images generated using the template library from test set of ImageCAS[53]. The framework randomly selects a template and a mask from the library and processes the mask through MGM-based geometric deformation. By integrating TCDM and SSV, synthetic images with corresponding confidence maps are systematically generated. The results demonstrate that FCaS preserves complete structural continuity across axial, sagittal, and coronal planes without anatomical discontinuities. Meanwhile, the synthesized images also simultaneously achieve intensity distributions closely matching real images. Confidence maps shown in Fig. 5 demonstrates differential reliability patterns, with fine-grained mask regions displaying higher confidence values and unmasked areas showing reduced certainty. When applied to downstream segmentation pre-training, models trained with confidence maps show enhanced focus on high-confidence cardiac structures, effectively suppressing attention to ambiguous background areas.

### 7.2. Segmentation Evaluation and Feature Distribution

Figure 6 visually presents Tab. 2 from the main text through bar chart comparisons. These comparisons clearly show that our synthetic images provide effective assistance to downstream pre-training models when real data is scarce. Compared with other methods, FCaS demonstrates greater performance improvement in pre-training tasks, particularly under data-limited conditions.

To better verify the realism, we employ t-SNE[13] to visualize the distributions of features extracted from 750 synthesized images from different methods. Specifically, feature representations for visualization are extracted from the middle hidden layer of nnU-Net, which is pre-trained on the training set of ImageCAS [53]. Meanwhile, the feature distributions of real data is used as the baseline. As illustrated in Fig. 7, we depict the distribution in three groups: unconditional, with surroundings, and without surroundings, respectively, which is consistent with the Tab. 1 in the main paper.

Compared to conditional methods, unconditional approaches[8, 24, 42] exhibit feature embeddings that deviate significantly from real data (green) and display large inter-class variances, resulting in scattered point clusters. This phenomenon arises from the lack of topological constraints provided by masks. Among conditional methods, DiffInfinite[1] exhibits worse spatial compliance with mask guidance and large intensity deviations. Other methods demonstrate closer proximity to features of real data (green), with fewer outliers due to the guidance of topological constraints from the conditional mask. Specifically, dat (red) generated from our FCaS shows the most compact clustering and nearest distance from real images, which further demonstrating our qualitative visual analysis. Notably, MAISI[10] achieves comparable results in “with surroundings” setting but exhibits distribution drift in “without surroundings”, which reveals that most methods display increased dispersion and feature space deviation when lacking surrounding tissue context.

Overall, the visualization results further confirm that FCaS synthesizes 3D fine-grained cardiac images with feature distributions closely resembling real data. This not only validates geometric fidelity but also ensures semantically accurate representations, enhancing the effectiveness of downstream pre-training tasks.

### 7.3. The MGM to Generate Different Masks

As shown in Fig. 8, we employ MGM to synthesize masks, thereby providing TCDM with diverse and high-quality image generations. The six representative cases displayed are generated through affine transformations (rotation, scaling, shearing, translation) and non-rigid transformations applied to original masks. It is observed that these derived masks

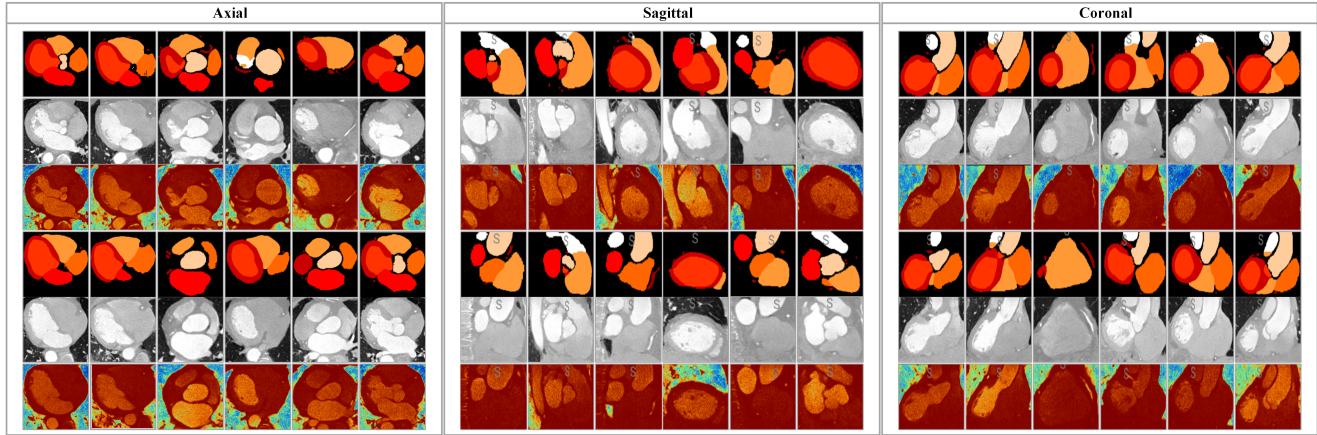


Figure 5. Additional visualization results of FCaS. Three distinct perspectives are presented to demonstrate the given mask and corresponding generated images as well as confidence maps.

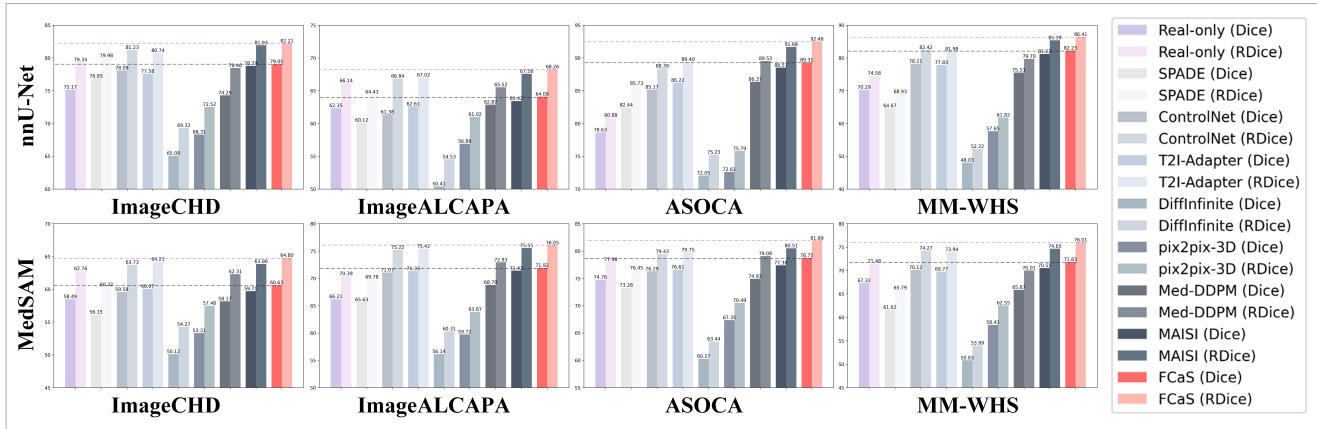


Figure 6. Comparative bar plots of pre-training performance metrics across four public datasets for different methods. Downstream segmentation models pre-trains using FCaS-synthesized data and subsequently fine-tunes with limited real data, achieving significant improvements in both Dice and RDice metrics.

preserve inherent topological relationships (e.g., coronary artery-ventricle positional alignment). Compared to direct deformations on images which often introduce localized expansions or depressions violating global human anatomy, our MGM applies deformations exclusively to fine-grained masks. This methodological distinction ensures images generated using these masks as references maintain structural integrity in surrounding tissues while achieving both topological preservation and morphological heterogeneity through using random parameters. Such MGM-generated masks not only maintain topological consistency but also introduce morphological diversity, effectively supporting precise structural synthesis in the FCaS framework.

#### 7.4. Manual Evaluation from Clinical Experts

In addition to evaluation quality of synthesized image via different metrics, we invite two experts with extensive clin-

ical experience to systematically score and rank the synthetic images generated by different methods. Specifically, we select synthesized images from 11 conditional and unconditional models for manual evaluation. Each model includes 200 images synthesized with surroundings and 200 images synthesized without surroundings. Synthesized images generated from the same reference by all 11 models are compared together. In other words, each evaluation bag contains 11 different synthesized images, and the experts are required to score them individually. The evaluation is conducted based on five key criteria: Visual Realism, Inter-layer Continuity, Topological Consistency, Coronary Detail Preservation and Morphological Heterogeneity. Within each evaluation bag, models are ranked according to their scores, where a rank of 1 indicates the best performance, and a rank of 11 represents the worst. Therefore, a lower rank value indicates better model performance.

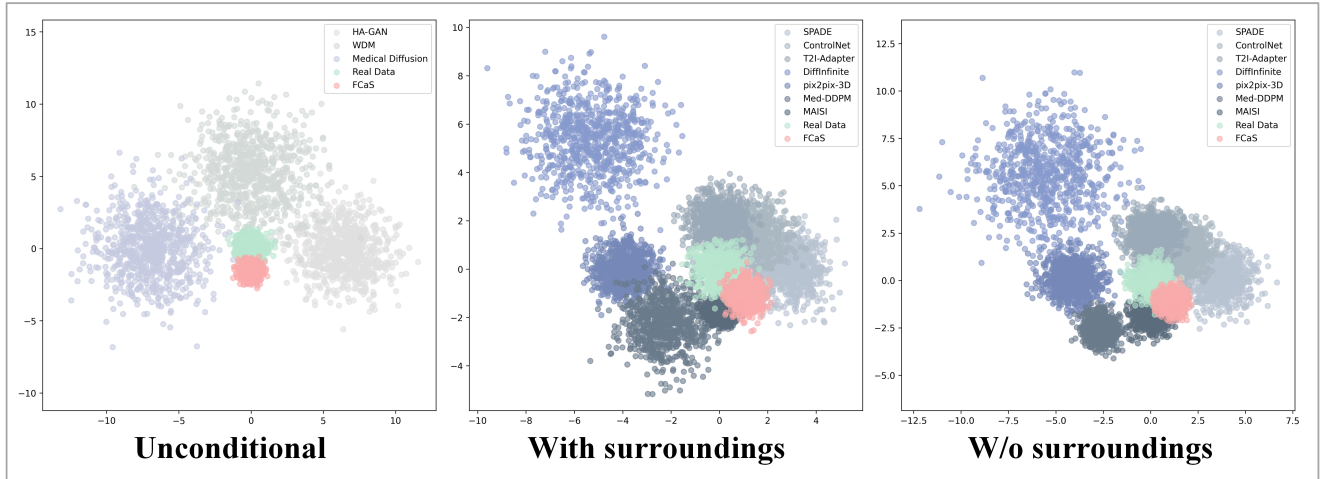


Figure 7. Scatter plots comparing feature distributions of data synthesized by unconditional versus conditional methods.

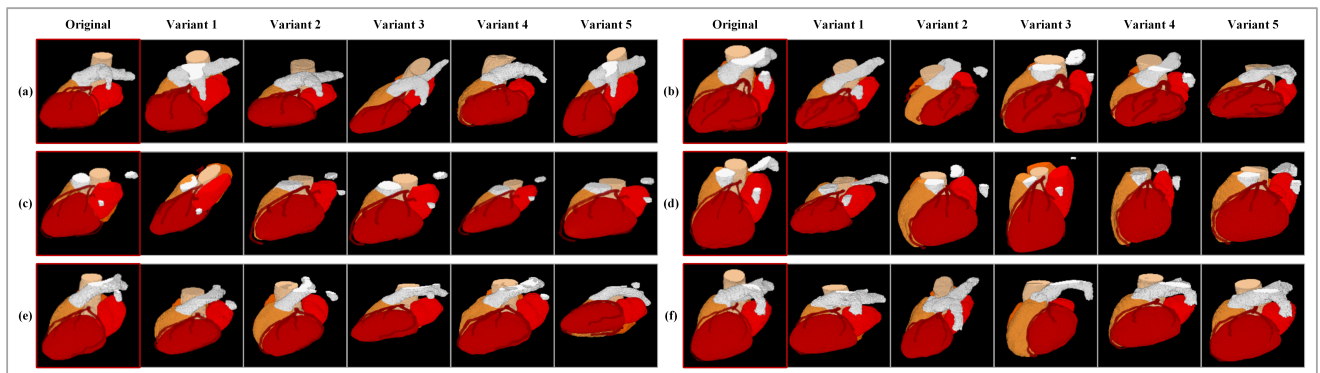


Figure 8. The topologically consistent and morphologically heterogeneous masks synthesized by MGM.

We compute the mean and variance of the ranks for each model across different evaluation bags and visualize the results using box plots. As illustrated in Fig. 9 (a) and (b), a lower position and shorter length of the box indicate that the synthesized images from the corresponding model achieve better rankings (*i.e.*, lower rank values) across multiple evaluation bags. Generally speaking, the proposed FCaS demonstrates remarkable performance. Meanwhile, as shown in Fig. 9 (c), we depict the radar chart comparing different models based on the scores of five key criteria used in the manual evaluation. It is obvious that our FCaS achieves the best performance, establishing the largest pentagon in the radar chart.

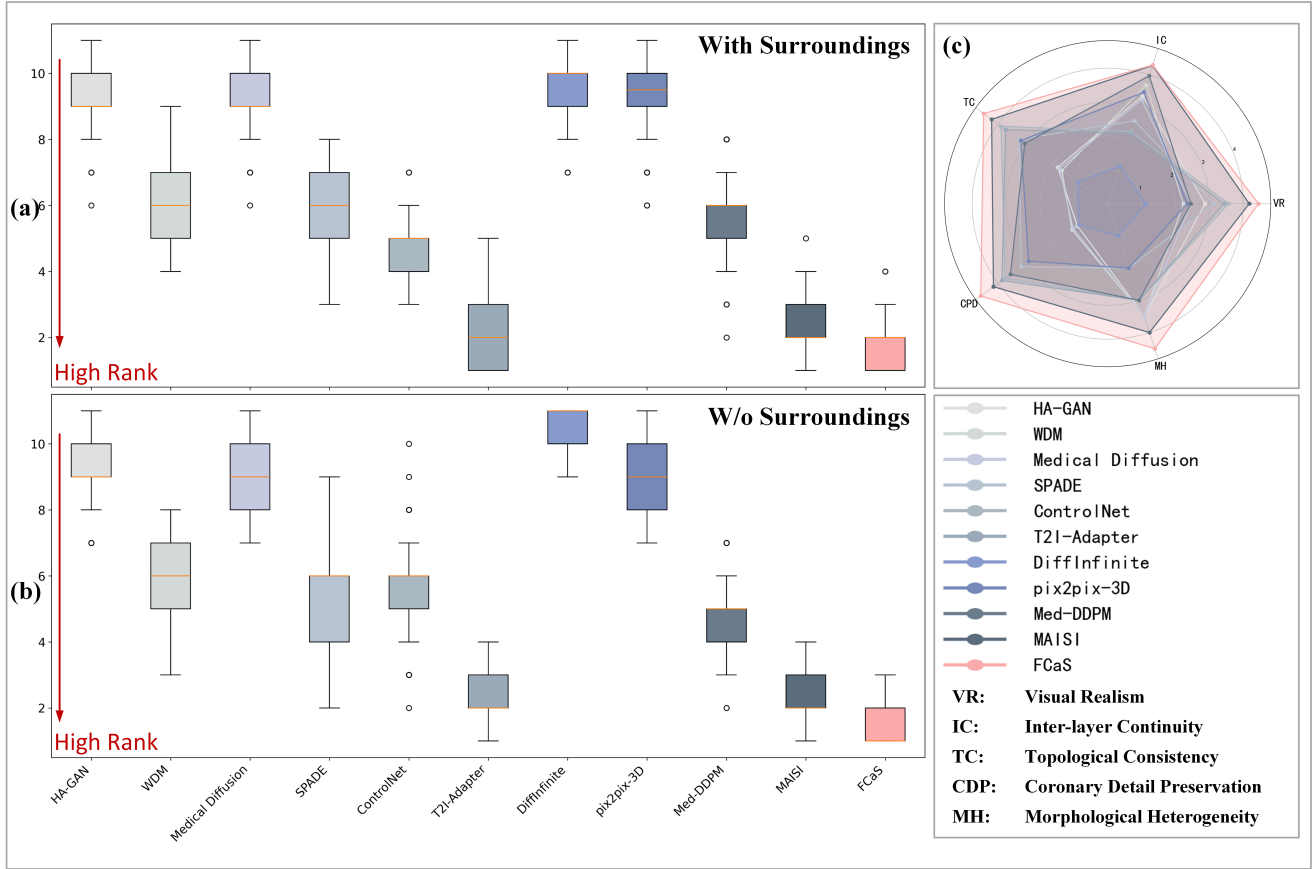


Figure 9. Visualization of clinical experts scoring and ranking results. (a) and (b) present box plots of ranking statistics (mean  $\pm$  standard deviation), demonstrating consistent top-tier rankings for FCaS. (c) employs a radar chart to compare synthesized images across methods, showing that FCaS-generated images achieve significantly higher expert scores compared to other methods.